



The Role of a Rock Discontinuity's Micro-structure and Aperture on the Detection of Seismic Precursors to Shear Failure

Hala El Fil¹ · Laura J. Pyrak-Nolte^{1,2,3} · Antonio Bobet¹

Received: 31 December 2022 / Accepted: 18 November 2023

© The Author(s), under exclusive licence to Springer-Verlag GmbH Austria, part of Springer Nature 2023

Abstract

Whether shear failure will occur along a fracture or joint depends on the nature of the two fractures surfaces, matched or mismatched, the asperity distribution, and surficial geochemical properties. Here we examine if the nature of the discontinuity surfaces affects observations of geophysical precursors to failure, specifically the effect of aperture, asperity distributions, and surficial chemistry. Laboratory experiments were performed on specimens composed of two gypsum blocks in contact with each other that had either well-matched or mismatched surfaces. Direct shear experiments were conducted under normal stresses of 2 and 5 MPa, while compressional and shear wave ultrasonic signals were transmitted across the discontinuity to monitor slip along the discontinuity. Seismic precursors to shear failure were detected for all well-matched discontinuities for all normal stresses. However, seismic precursors appeared only under the higher normal stress for mismatched discontinuities. The interplay between wave transmission, the degree of mismatch, and discontinuity's micro properties was assessed through 3D CT in-situ X-ray scans, micro-indentation testing, and scanning electron microscopy and electron X-ray diffraction. The data indicated that for the mismatched discontinuities used in this study: (1) the void aperture was large, so significant shear displacement was needed to interlock and damage the asperities; and (2) the micro-hardness of the asperities was larger than that of the well-matched discontinuity. The results suggest that monitoring changes in transmitted wave amplitude across a discontinuity is a promising method for predicting impending failure for rock discontinuities but works best when there is sufficient contact between the rock surfaces.

Highlights

- A series of direct shear experiments was conducted on well-matched and mismatched rock discontinuities.
- Seismic precursors to shear failure were observed for well-matched discontinuities at different normal stresses.
- Seismic precursors to shear failure were only observed at higher normal stress for mismatched discontinuities.
- The interplay between wave transmission, degree of mismatch, and micro-properties were examined through CT in-situ scan, μ -indentation, SEM, and EDX.

Keywords Rock discontinuities · Precursors · Seismic waves · X-ray tomography

✉ Hala El Fil
hala.elfil4@gmail.com

¹ Lyles School of Civil Engineering, Purdue University, West Lafayette, IN 47907, USA

² Department of Physics, Purdue University, West Lafayette, IN 47907, USA

³ Department of Earth and Atmospheric Sciences, Purdue University, West Lafayette, IN 47907, USA

1 Introduction

Discontinuities in rock masses represent planes of weakness that may result in the failure of structures built on or near fractured rock masses, causing casualties and economic losses. It is essential to investigate and understand the shearing mechanism of rock discontinuities to provide foundational knowledge to develop geophysical methods to detect impending slip or failure. Recently, potential seismic precursors to an ice-rock

slope failure in the Himalayas were detected approximately 3 h before a catastrophic failure (Tiwari et al. 2022). The seismic stations near the avalanche source generated reliable data with a high signal-to-noise ratio and showed increased signal amplitude prior to failure. Previous laboratory studies have investigated the shear behavior of well-matched discontinuities by conducting direct shear experiments that employed geophysical tools such as active ultrasonic monitoring (Chen et al. 1993; Hedayat and Hinton 2017; Hedayat and Walton 2017). For example, Chen et al. (1993) examined the shearing behavior of granite samples with pre-existing discontinuities while employing active seismic monitoring. They distinguished between stable sliding and stick–slip behavior by observing the amplitude of shear waves. The amplitudes decreased during stable sliding and increased rapidly before or at slip. Hedayat et al. (2014) employed active seismic monitoring to investigate the shearing response of rough discontinuities in gypsum and Indiana limestone. They were able to detect seismic precursors to shear failure in the form of peaks in the normalized transmitted amplitude and corresponding troughs in the normalized reflected amplitude in both rocks. Also, various studies successfully applied machine learning to predict the time remaining before slip took place in the laboratory, using acoustic emission data recorded by running double direct shear experiments on fault gouges (Johnson et al. 2021; Rouet-Leduc et al. 2017). Hulbert et al. (2019) also used machine learning with acoustic emission data from shearing experiments on quartz fault gouge. They were able to predict the time and magnitude of laboratory-induced earthquakes.

Converted seismic waves, compressional (P) to shear (S), or P-S, and shear (S) to (P), or S-P, have also been used to detect precursors to failure. The use of converted waves to detect slip follows the work of Nakagawa et al. (2000) who detected converted waves (P-S and S-P) caused by voids that were preferentially oriented from shearing along the fracture plane. These converted waves have been observed and used as seismic precursors to shear failure while shearing sandstone samples (Gheibi et al. 2021) and saw-toothed discontinuities in gypsum (El Fil et al. 2021). Converted seismic signals have also been employed to detect shear failure and shear crack initiation in pre-cracked limestone specimens (Modiriasari et al. 2018, 2020).

In this paper, we refer to well-matched discontinuities as those in which the two surfaces are in close contact over a significant area. Conversely, we refer to mismatched discontinuities as those in which the two surfaces are not in close contact over a significant area. These definitions are consistent with the terminology introduced by Hoek and Brown (1980). The research efforts cited above focused on shear along well-matched discontinuities. However, in nature, rock discontinuities are not always perfectly matched because chemical and/or physical processes can weather the fracture surfaces (Singh and Basu 2016), or tectonic forces,

seismic events, or excavations may cause movements in pre-existing discontinuities (Cheng Tang et al. 2016). Despite the extensive research conducted so far to understand the shearing processes of rock discontinuities (Kulatilake et al. 1995; Singh and Basu 2018; Xia et al. 2014), and to develop methods to detect impending shear failure (Gheibi et al. 2021; Hedayat et al. 2014; Scuderi et al. 2016), the behavior of mismatched discontinuities is still not well understood.

In this paper, results from direct shear experiments conducted on gypsum specimens with two types of frictional discontinuities, each with different micro-structure, micro-strength, and degree of matching, are presented and discussed. First, we demonstrate that seismic precursors to shear failure of well-matched discontinuities can be detected through geophysical techniques, which agrees with the previous findings of Hedayat et al. (2014). Second, we show that seismic precursors to shear failure for mismatched discontinuities cannot be detected at low normal stress but are detected at higher normal stresses. Third, we discuss the interplay that exists between wave transmission, precursor detection and discontinuity micro-properties using data from: (1) 3D CT in-situ X-ray scans to quantify the degree of mismatch with normal stress; (2) micro-indentation testing to measure the strength of the asperities; and (3) Scanning Electron Microscopy (SEM) and Electron X-ray Diffraction (EDX), to characterize the microstructure and chemical composition of each type of discontinuity.

2 Sample Preparation and Experimental Program

2.1 Direct Shear Experiments

All the laboratory specimens were made of gypsum, a rock-model material (Bobet and Einstein 1998; Mutlu and Bobet 2006). Each specimen was composed of two independent

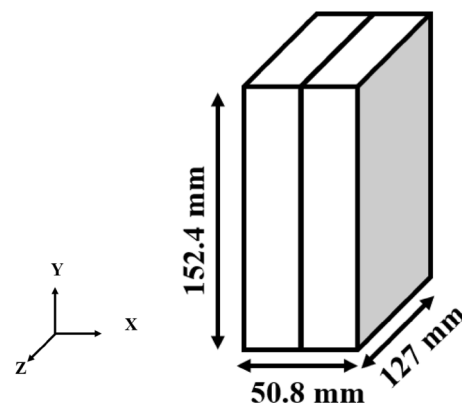


Fig. 1 Schematic of the specimen dimensions

prismatic blocks (length = 152.4 mm, width = 127 mm, and thickness = 25.4 mm, as shown in Fig. 1) fabricated in the laboratory following a previously documented protocol (Bobet 1998; Choi 2013; Hedayat 2013). First, 11.43 g of diatomaceous earth and 400 cm³ of water were mixed in a blender at a low speed (54 rpm) for 30 s. Next, a 1000 g of gypsum Hydrocal B11 powder was added to the mixture and blended at a low speed (54 rpm) for 30 s and then at a high speed (180 rpm) for 4.5 min. The mixture was then poured into a mold with a grit 36 sandpaper (483 μm grain size) at the bottom. Afterward, the mold was vibrated at high speed (100 rpm) for 5 min to remove the air bubbles. After an hour, the hardened sample was turned over, and a second gypsum mixture was poured over the rough surface of the first block. Before pouring, care was taken to apply a thin layer of a mold release agent to the rough surface of the first block to prevent adhesion between the blocks after curing. The nature and the amount of the mold release agent affected the specimen surfaces. Specimens were prepared either with a water or an oil-based release agent. Specimens prepared with a water-based release agent (2418 Dow Corning) are referred to as G_W in the following, while those prepared with an oil-based release agent (Duoguard) are labeled G_O. A very thin layer of the water-based release agent was sufficient to separate the two blocks after preparation. Conversely, the oil-based release agent required the application of a larger amount of release agent to separate the two blocks without damaging the asperities. As will be discussed later, specimens prepared with the water-based release agent (G_W) created well-matched discontinuities, while specimens prepared with the oil-based release agent (G_O) resulted in mismatched discontinuities with stronger asperities from chemical processes than in the well-matched case.

The experimental setup is presented in Fig. 2a–c and includes a biaxial apparatus composed of a flat jack and a reaction frame to apply the normal stress. The flat-jack pressure was controlled using an electronic feedback loop control (CC8 multi-test control machine) to ensure that the imposed normal load was constant throughout the experiment. Two normal stresses were used: 2 MPa and 5 MPa. An Instron machine was used to impose the shear load at a displacement-controlled rate of 8 μm/sec. The experimental setup also included an ultrasonic seismic system composed of a National Instruments (NI) PXI-1042 chassis with two multiplexer switches (NI TB-2630) and a 68-pin NI TB terminal block that connects the chassis with the relay switch. Ultrasonic transducers (Olympus V153RM for shear & V103RM for compression) with a diameter of 11 mm and a central frequency of 1 MHz were used in this research. Square pulses with an amplitude of 100 V and a repetition rate of 1 kHz were generated with an Olympus 5077PR pulse generator to excite the piezoelectric transducers. The sensors were housed inside steel blocks on each side of the

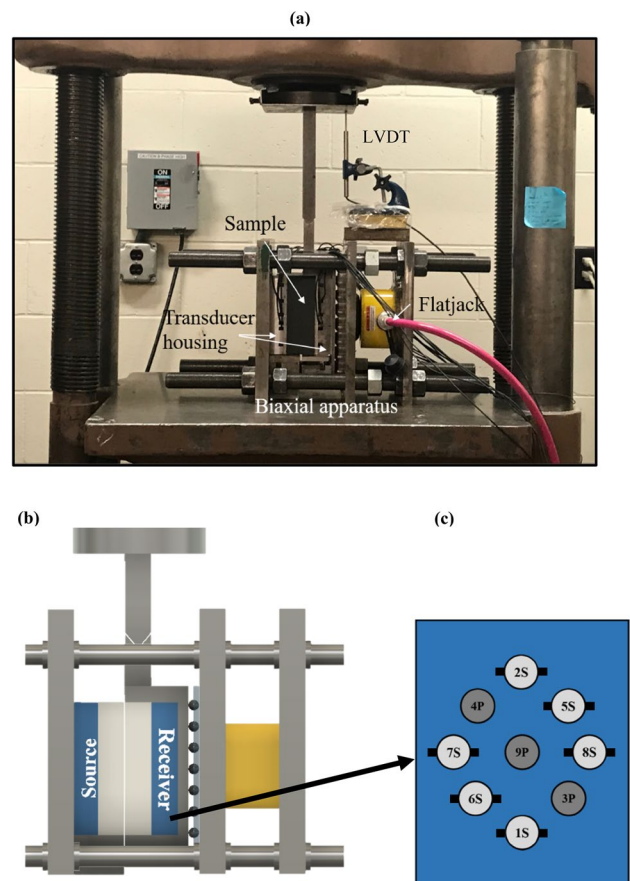


Fig. 2 Experimental Setup. **a** Photograph of Test setup; **b** schematic of the direct shear apparatus; **c** transducers' layout

specimen (Fig. 2b). Each housing contained 9 shear and compressional ultrasonic transducers. Figure 2(c) presents the layout of the transducers (“P” for compressional and “S” for shear transducers, polarized in the horizontal direction, i.e., perpendicular to the direction of shear). During the tests, seismic signals were transmitted across the specimens at a rate of 100 Msamples/second, i.e., 10,000 data points, yielding 0.01 microseconds per point. At least two experiments were conducted for each type of frictional discontinuity to test repeatability.

2.2 Micro-scale Characterization of the Discontinuity Surfaces

2.2.1 Micro-structure and -composition Experiments

Microstructure characterization and chemical composition of the material were investigated along the discontinuity surfaces using an FEI Nova NanoSEM scanning electron microscope (Life Science Microscopy facility at Purdue University). Imaging was performed on a subsection of the joint surface taken from each type of specimen (G_O

and G_W), using a 5 kV voltage, a spot size of 3, a working distance of 5 mm, and a magnification range between $1000\times$ and $7000\times$. Prior to scanning, the surfaces of the sample were coated with platinum by employing a Cressington turbo-pumped sputter coater to avoid charging the specimen surface under the microscope. EDX scans were captured at a 10 kV voltage, a spot size of 3, at a working distance of 5 mm. A Monte Carlo simulation was conducted to determine the electron trajectory using Winxray (Demers et al. 2002), and to verify that we are scanning surficial properties of the asperities. The output of the Monte Carlo simulations showed that the transmitted electrons had a bell-shaped trajectory with a depth of $\approx 1.8\ \mu\text{m}$ and a width of $\approx 2.7\ \mu\text{m}$, indicating that the chemical elements correspond to the elements encountered on the surface.

2.2.2 Micro-indentation Experiments

The strength of the discontinuity surfaces was characterized through micro-indentation. A Hysitron Tribo-indenter Nano-indenter 950 (load capacity $\approx 14,000\ \text{N}$) was used (Material's engineering laboratory at Purdue University) to quantify the micro-hardness of the asperities prepared with both types of mold release agents. The selected indenter had a conical tip with a tip diameter of $10\ \mu\text{m}$ and a 62° tip angle. The size of the indenter was chosen such that a representative volume of material was tested rather than a single needle or a void between needles. Micro-indentation tests were conducted on rough and smooth surfaces (grit 36 sandpaper roughness) prepared with oil and water-based release agents (G_O and G_W specimens). Although it is recommended that indentations are made on smooth and well-polished samples, based on ASTM E384 (2005) and ASTM E2546 (2007), indentations were also carried out on the rough surfaces to quantify the asperity hardness. Because of the difficulty in indenting a rough surface, only five indentations were completed on each type of surface, while 25 indentations were conducted on smooth surfaces.

2.2.3 Fracture Imaging

Voids and asperity contact imaging was performed with an in-situ stress rig in a 3D X-ray microscopy; see Fig. 3(a). Because of equipment size limitations, specimens were made of two blocks, each with dimensions 19 mm in length, 18 mm in width, and 6 mm in height. Preparation of the specimens followed the same process described in Sect. 2. Figure 3(b) shows the G_W and G_O specimens. At least three specimens of each type (G_W and G_O) were tested and imaged. The specimens were scanned using

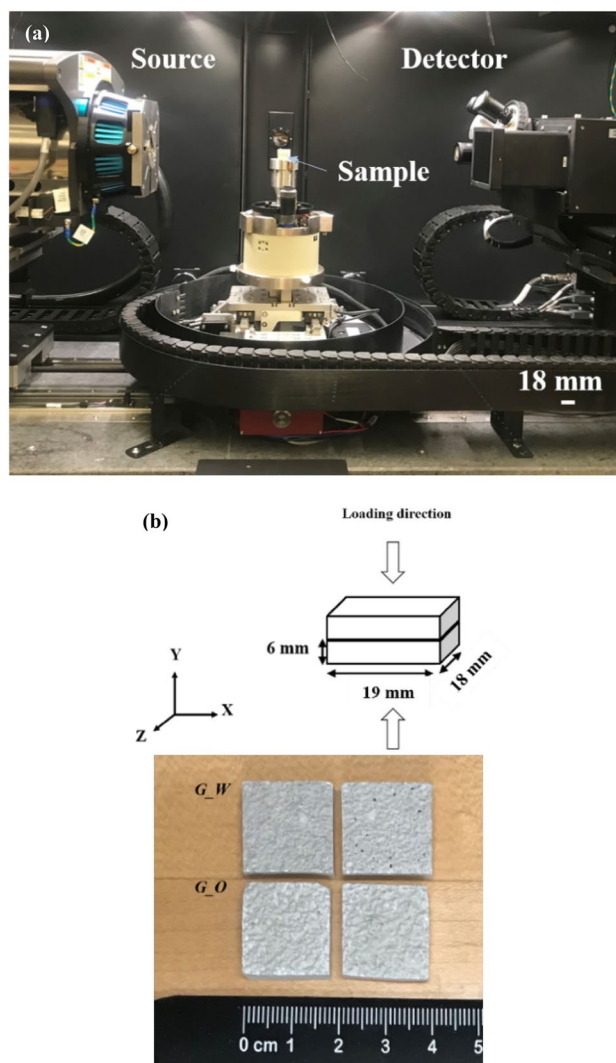


Fig. 3 Surface Contact and Void Characterization. **a** 3D X-ray experimental setup; **b** G_W (top) and G_O (bottom) specimens and schematic showing the loading direction

a 3D X-ray microscope (XRM), Model Zeiss Xradia 510 Versa. As shown in Fig. 3(a), each specimen was placed in a Deben CT5000 loading stage (load capacity of 5000 N), positioned between the X-ray source and the X-ray detector. The scans were conducted with a resolution of $\approx 23\ \mu\text{m}/\text{pixel}$. The energy and power of the scans were 160 kV and 10 W, respectively. Each specimen was placed between the source and the detector with source and detector distances of 100 mm and 200 mm, respectively. The scans had an exposure time of 1 s for 3201 projections, a $0.4\times$ magnification factor, a bin size of 2, and no filter (air) was used. The specimens were loaded in the normal direction [y-direction, as shown in the schematic in Fig. 3(b)] at a loading rate of 0.1 mm/min.

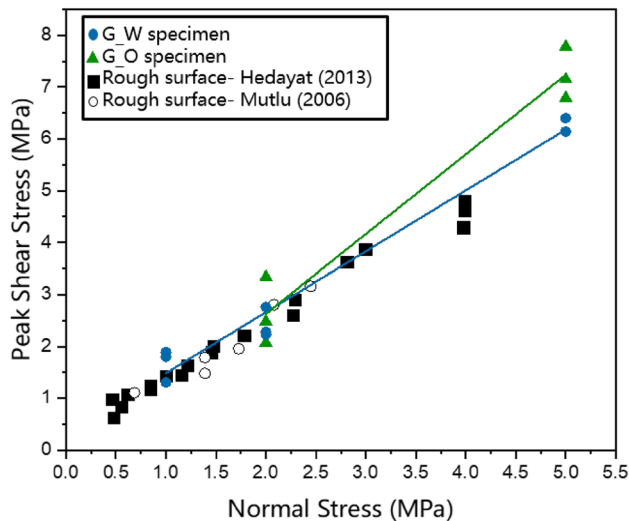


Fig. 4 Peak shear stress as a function of normal stress with data from previous researchers (Hedayat 2013; Mutlu and Bobet 2006)

3 Results and Discussion

3.1 Mechanical Response

Figure 4 shows the peak shear stress as a function of normal stress from the experiments on specimens with G_W (water-based release agent), blue circles, and G_O (oil-base release agent), green triangles. G_O and G_W specimens were made of gypsum. The peak friction angle for G_O specimens was $\approx 56.9^\circ$, while for the G_W specimens, it was $\approx 49.6^\circ$. The peak friction angle obtained for the G_W specimens is in good agreement with previous work (Hedayat 2013, frictional angle of $\approx 50^\circ$, black squares in the Fig. 4, and Mutlu and Bobet 2006, obtained a frictional angle of 51.4° , open circles). The residual friction angle of both G_W and G_O specimens was similar, measuring at approximately 41° .

The average peak shear stress of G_W specimens at a normal stress of 2 MPa was ≈ 2.49 MPa with a standard deviation of ≈ 0.29 , and of G_O specimens, ≈ 2.63 MPa and a standard deviation of ≈ 0.65 . The difference of the average peak shear strength between the two types of specimens was 5.5%, indicating that the surface treatment had a small influence in the peak shear strength at low (2 MPa) confinement. At a normal stress of 5 MPa, the average peak shear stress of G_W specimens was ≈ 6.27 MPa with a standard deviation of 0.18, while that of G_O specimens was ≈ 7.24 MPa with a standard deviation of 0.50. This shows a more significant difference in the peak shear strength of both specimens, with a difference in the average peak shear stress of $\approx 14.4\%$. The cause for the observed differences in shear strength was explored by examining the surface properties

of the two types of discontinuities (i.e., G_W and G_O), and is discussed later.

3.2 Geophysical Response

The normalized transmitted amplitudes from representative transducers at the top (5S), middle (9P), and bottom (1S) regions of the specimen are presented in Fig. 5 (only three representative transducers are shown for clarity). The data were obtained by performing a wavelet analysis (Combes et al. 1989; Nolte et al. 2000) and extracting the amplitude of the dominant frequency for each signal at each normal stress. The transmitted amplitudes are shown as a function of shear displacement for a representative G_W specimen, Fig. 5(a–b), and G_O specimen, Fig. 5(c–d), sheared under constant normal stresses of 2 and 5 MPa. Figure 5 also includes the shear stress as a function of the shear displacement on the secondary y-axis. For the G_W specimen, at 2 and 5 MPa, Fig. 5(a–b), the data show that as the shear stress increases, the normalized transmitted amplitude increases. This increase is caused by an increase in both normal and shear fracture-specific stiffnesses during shear, which has been shown to enhance transmission (Choi et al. 2014; Pyrak-Nolte et al. 1990; Pyrak-Nolte 2018). The transmitted amplitude then reaches a peak prior to the peak shear stress and then decreases. The decrease in the normalized transmitted amplitude is caused by a decrease in coupling between the two blocks that form the discontinuity, which is interpreted as damage to the asperities. Thus, the change in amplitude can be used as an indicator of impending failure; that is, as a precursor to failure. Transducer 5S in Fig. 5(b) shows a sharp drop in amplitude at about 1.26 mm of displacement. This is normally the result of a crack in the matrix that is orthogonal or perpendicular to the discontinuity's surface that occurred during shearing.

In contrast, for the G_O specimen, at a normal stress of 2 MPa, no precursors are observed; see Fig. 5(c). As expected, the normalized transmitted amplitude increases as the shear stress increases. However, the peak in amplitude occurs after the peak shear stress. However, precursors to failure were found for the test at a normal stress of 5 MPa, as shown in Fig. 5(d). As observed in Fig. 5(d), as the shear stress increases, the normalized transmitted amplitudes from all the transducers increase, then a peak in amplitude is reached before the peak shear stress is reached. This is similar to what was observed from the G-W specimens and is consistent with previous findings (Hedayat et al. 2014). The post-peak maxima observed for the G_O specimen, at a normal stress of 2 MPa, are associated with a delayed onset of damage to the asperities. The causes and mechanisms of the delay have been investigated through extensive work to characterize the discontinuity at the micro-scale.

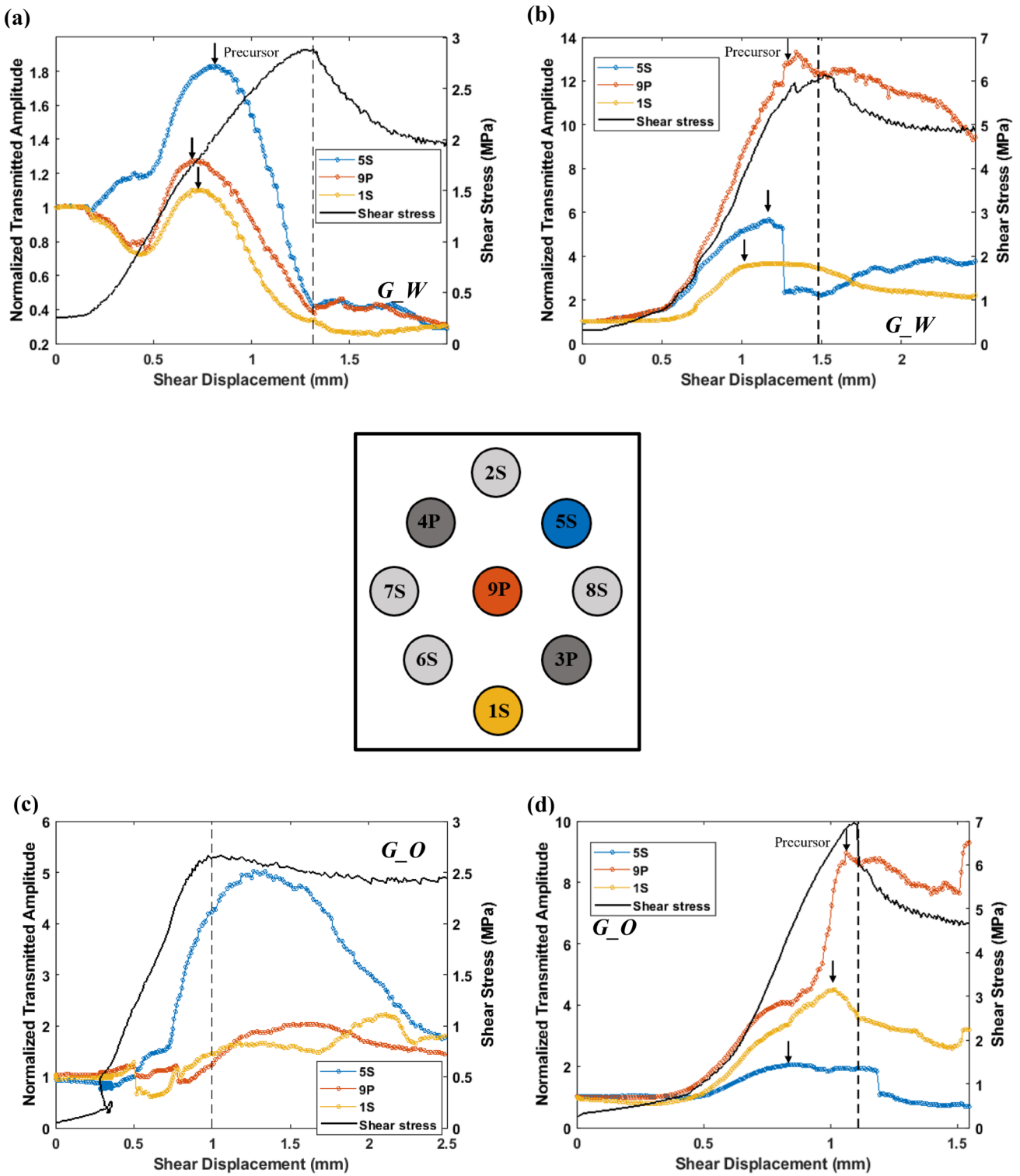


Fig. 5 Normalized transmitted amplitude for specimens prepared with a water release agent (G-W) at a normal stress of **a** 2 MPa and **b** 5 MPa; and with an oil release agent (G_O) at a normal stress of **c** 2 MPa and **d** 5 MPa. Normalized transmission plots and transducers are color-coded

3.3 Micro-scale Characterization of the Discontinuity Surfaces

A decrease in amplitude of the transmitted waves occurs when there is a loss of shear stiffness in the region sampled by the transducer either from asperity damage, dilation of the fracture or loss of shear contact between the surfaces. We hypothesize that the different chemicals applied to the surface of the specimen affected the (local) strength of the asperities. The sources of frictional strength are identified as: (1) basic frictional strength (i.e., residual strength) of the material of the surface; (2) strength of the material forming the asperities; and (3) joint roughness/dilation, i.e., the asperity height and shape distribution on the surface (Barton and Choubey 1977). To test our hypothesis, measurements were made to characterize the material composition, material strength, and roughness of the discontinuities.

3.3.1 Micro-structure and -composition

Representative SEM images of a rough surface prepared with grit 36 sandpaper are shown in Fig. 6 for specimens: (a) G_W, and (b) G_O. Crisp, needle-like structures were observed on the surface prepared with the water-based release agent (G_W), with needle lengths ranging from 0.4 to 15 μm and widths between 0.5 and 3.5 μm , as shown in Fig. 6(a). The needles were less distinct and more amorphous for the specimen prepared with the oil-based release agent (G_O), resulting in a microstructure, Fig. 6(b), that was smoother than that observed for the G_W specimen.

Table 1 Chemical composition of gypsum obtained from the manufacturer

Material	Weight (%)
Plaster of Paris ($\text{CaSO}_4 \cdot \text{H}_2\text{O}$)	> 85
Portland Cement (C_3S , C_2S , C_3A , and C_4AF)	< 10
Crystalline Silica	< 5

A chemical composition analysis was also performed with an Energy-dispersive X-ray spectroscopy (EDX) to determine if the release agents' nature affected the material's chemical composition on the surface. The chemicals in the gypsum specimens (no release agent) were obtained from the manufacturer of the Hydrocal B11 gypsum (Table 1). Figure 7(a) shows a typical chemical composition spectrum obtained from the EDX analysis, in blue for a G_W specimen, and in green for a G_O specimen, along with images of the scanned surfaces. The peaks observed in the graph in Fig. 7(a) represent distinct X-ray energies that correspond to specific chemical elements. The spikes were identified as carbon (C), oxygen (O), silicon (Si), sulfur (S), and calcium (Ca), the same elements listed in Table 1.

Figure 7(b) shows the chemical composition of the G_O (green) and G_W (blue) surfaces normalized with respect to the oxygen count (highest element count). The graph shows that almost all chemical elements were present in both scanned surfaces, except for magnesium which was only identified in G_O specimens but with minimal counts. As one can see, based on the EDX results, the two surfaces did not exhibit significant differences in chemical composition.

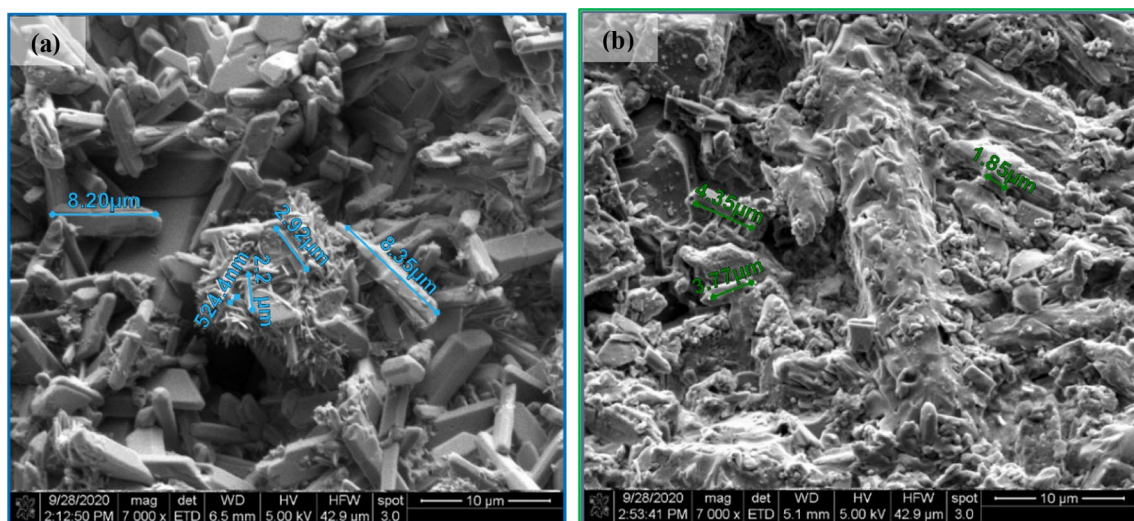


Fig. 6 SEM images of a rough surface prepared with: **a** water-based release agent (well-matched); and **b** oil-based release agent (mismatched) at a 7000 \times magnification

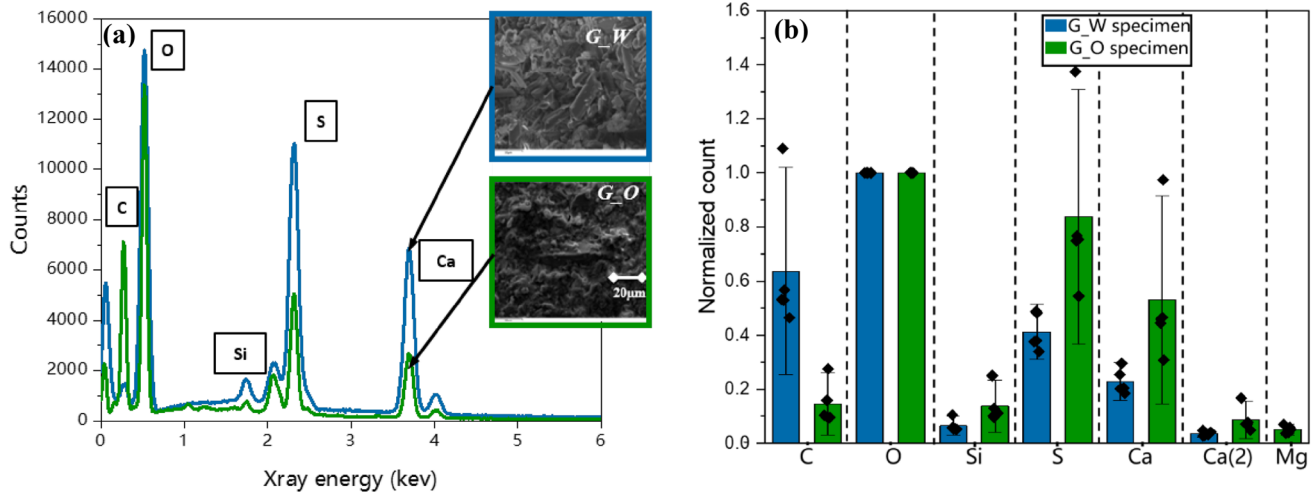


Fig. 7 Material on the surface of the discontinuities. **a** Chemical composition spectrum for a surface prepared with a water-based release agent, G_W, (blue), and oil-based release agent, G_O, (green); **b** Chemical elements on the surface of water-based, G_W,

(blue) and oil-based, G_O, (green) release agents, normalized with respect to oxygen count. The diamonds represent counts from the individual spectrum, and the error bars represent the standard error

3.3.2 Discontinuity's Micro-strength

The strength of the discontinuities surfaces was obtained through micro-indentation experiments. The micro-hardness for each indentation was computed using the following procedure (Fischer-Cripps 2011): first, the stiffness “*s*” was obtained, which is the slope of the linear portion of the unloading curve; then, the linear portion of the unloading curve was extended, and the point of its intersection with the x-axis was identified, which represents the contact depth *h_c*; finally, the contact radius (*a*) and the contact area (*A_c*) were calculated using Eqs. 1 and 2, respectively:

$$a = \sqrt{2R_i h_c} \tag{1}$$

$$A_c = \pi \times a^2 \tag{2}$$

where *R_i* is the indenter radius (5 μm).

The hardness was obtained by dividing the maximum load (*P_{max}*) by the contact area, as shown in Eq. 3:

$$\text{Hardness} = \frac{P_{\max}}{A_c} \tag{3}$$

Figure 8 shows the rough surface of a G_W specimen under the microscope: (a) before and (b) after indentation. The blurred regions in Fig. 8 are caused by the depth of focus during imaging. The roughness, i.e., the peaks and troughs of the asperities, have different heights causing some regions to be out of focus. The black dots observed in Fig. 8

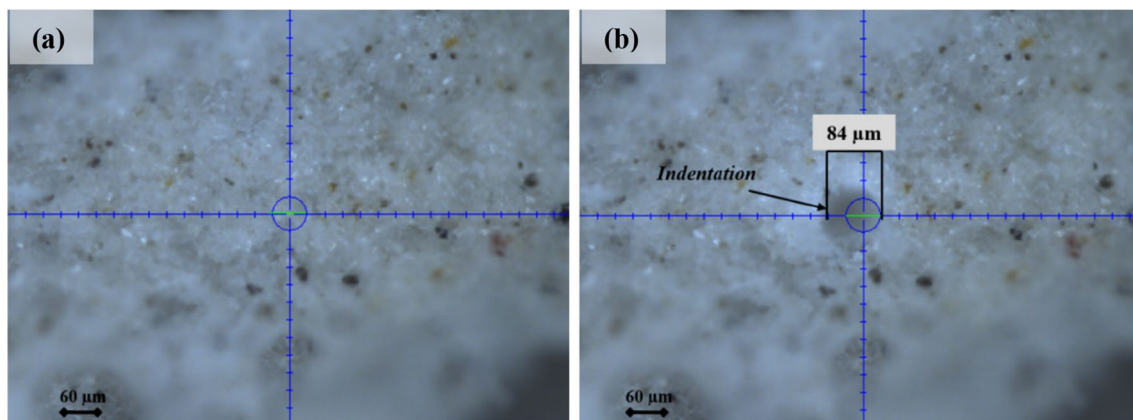


Fig. 8 Micro-indentation of a G_W specimen with a rough surface: **a** before; and **b** after indentation

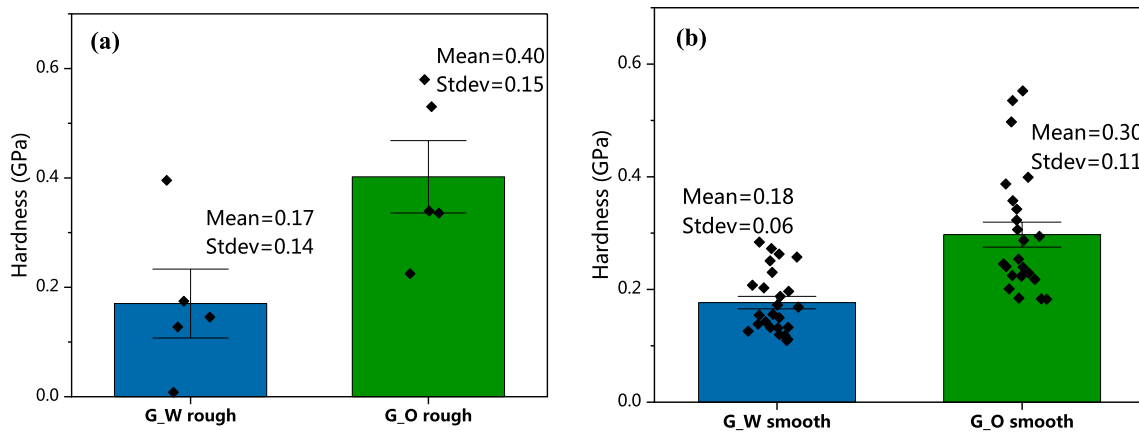


Fig. 9 Micro-hardness results of G_O and G_W specimens with **a** rough; and **b** smooth surfaces. The diamonds represent the hardness values of individual indentations performed, and the bars represent the standard error

are likely pores on the surface. Figure 8(b) shows that the indentation (blurry region behind the crosshair) had a diameter of $\approx 84 \mu\text{m}$, indicating that the indentation performed was adequate given that it was much larger than the size of a single crystal [0.4–15 μm in Fig. 6(a)]. The micro-indentation raw data (load versus indentation depth) are presented in Appendix A.

The micro-hardness values computed from the indentations performed are shown in Fig. 9. The G_O specimens with rough surfaces had a mean hardness of ≈ 0.40 GPa, while the G_W specimens had a mean hardness of ≈ 0.17 GPa, thus indicating that the asperities of the G_O specimen were at least two times harder than the G_W specimen.

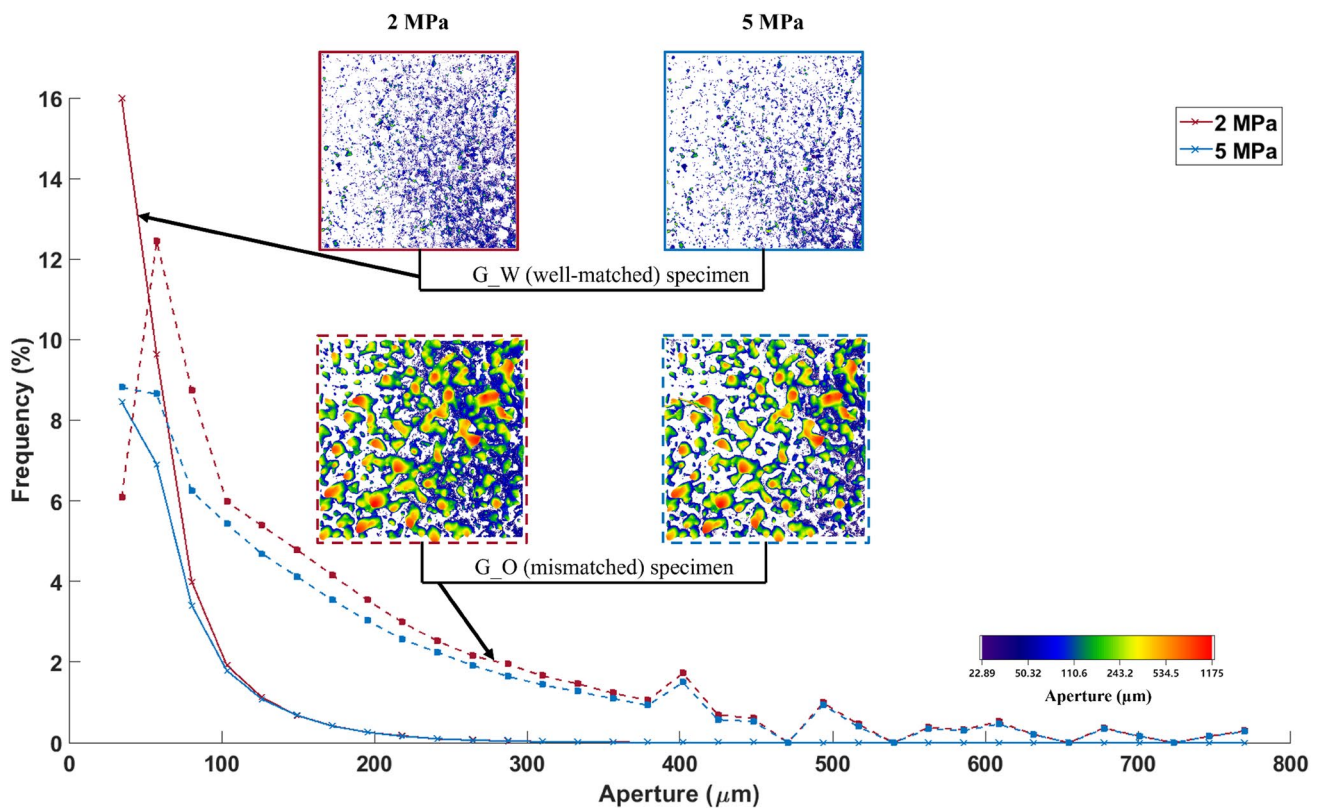


Fig. 10 Aperture height for **a–b** G_W; and **c–d** G_O specimens, at 2 MPa (maroon) and 5 MPa (blue) normal stresses with logarithmic color bar

As shown in Fig. 9(b), G_W specimens with a smooth surface had a mean micro-hardness of 0.18 GPa, while G_O specimens, also with a smooth surface, had a mean micro-hardness of 0.30 GPa, about 50% larger than the G_W specimen, but with larger variability. The results show that the asperities present on the G_W specimens are weaker when compared to those on the G_O specimens.

3.3.3 Fracture Imaging

The 3D CT Xray collected images obtained from experiments discussed in Sect. 2.2.3, were post-processed using Objective Research Systems (ORS) Dragonfly 4.0 (2020) software for data analysis. A built-in machine learning module in Dragonfly ORS 4.0 was employed for the rock matrix and discontinuity segmentation. The segmentation engine was chosen as the “extra trees” algorithm (Geurts et al., 2006). The model outputs two regions of interest: (1) the aperture; and (2) the surrounding rock matrix.

Figure 10(a–b) shows the distribution of apertures for both specimens, G_W (well-matched) in solid lines and Fig. 10(c–d) for G_O (mismatched) in dashed lines, at

normal stresses of 2 and 5 MPa. There is a distinct difference between the results of both specimens. The aperture distribution for G_W specimens ranged between 22.89 μm and $\approx 200 \mu\text{m}$, while the distribution of G_O specimens showed apertures up to 800 μm . The large apertures in the G_O specimen did not close as the normal stress increased. This is attributed to the mismatch in the geometry of the asperities between the two surfaces that compose the discontinuity. For the well-matched discontinuity specimen (G_W), the aperture distribution shifts to the left (decrease in aperture height) with increasing stress because of the decrease in aperture with stress and increase in the contact area. For the (mismatched) G_O specimen, the apertures between 22 and 300 μm decrease with an increase in normal stress, but the larger apertures ($> 300 \mu\text{m}$) remain at all normal stresses. This is likely linked to the shape of the aperture and how it deforms under load, and to the surface mismatch.

The insets in Fig. 10, i.e., Fig. 10(a–d), are contour plots of the fracture aperture. Figure 10(c–d) shows that the apertures from the G_O specimen (mismatched discontinuity) are connected at low normal stress (2 MPa) and are quite large ($\approx \geq 0.5 \text{ mm}$). As the normal stress increased to

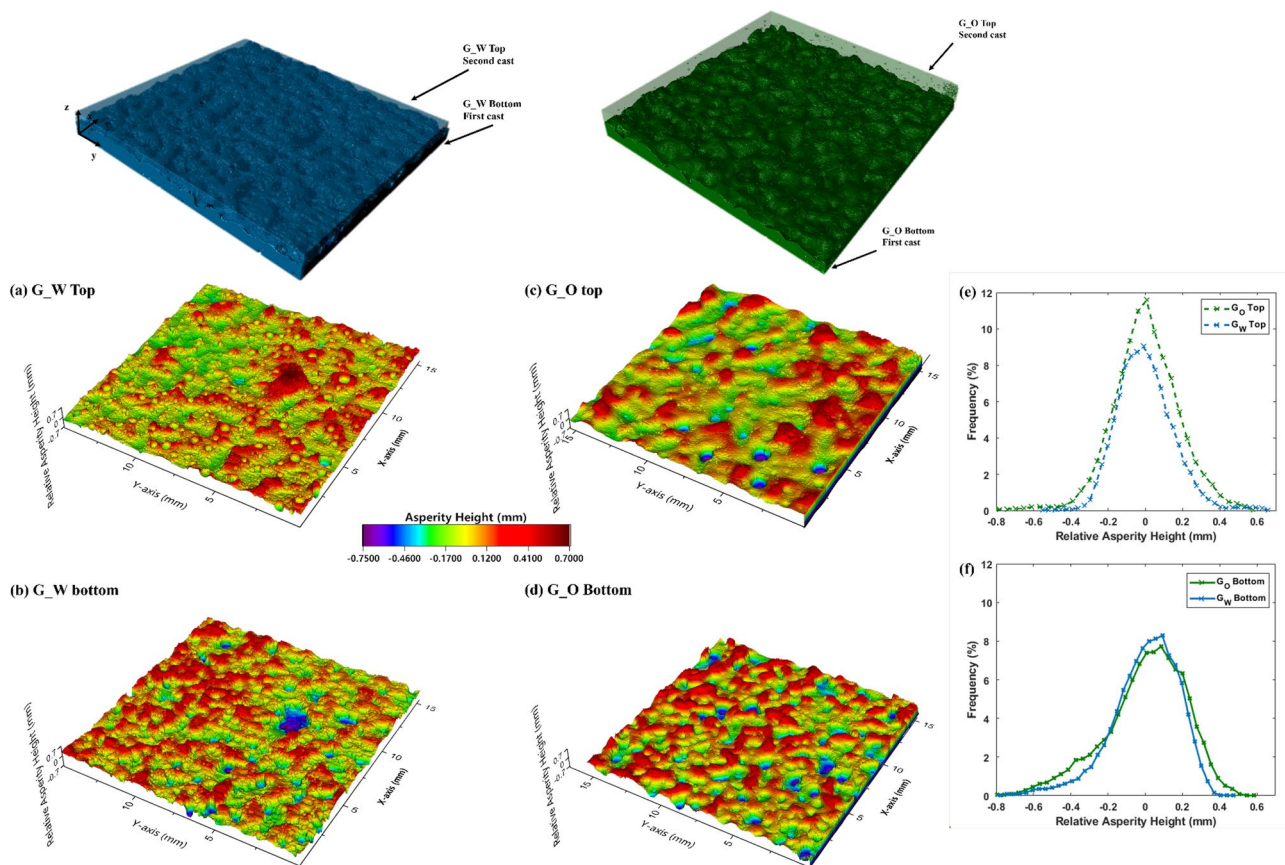


Fig. 11 Asperity height reconstruction for **a–b** G_O, and **c–d** G_W specimens; **e–f** asperity height distributions for top and bottom half-spaces, respectively

5 MPa, the apertures became disconnected, but the large apertures were still present. This contrasts with the change in apertures for the G_W specimen (well-matched discontinuity) in Fig. 10(a–b), where the apertures are quite small (mostly < 150 μm), even at low normal stress. The reason for larger apertures observed in G_O specimens is due to the fact that the oil between the troughs of the asperities is not absorbed and thus, when casting the second block on top of the first block, this results in a mismatched discontinuity.

The asperity heights and geometry of both types of discontinuities are shown in Fig. 11(a–d). Results from the bottom (first cast) and top (second cast) halves of the discontinuity are shown separately. Note that in the plots, the mean asperity height was subtracted from each data point to have the mean centered at zero. Figure 11(e–f) show that the G_O specimen had a wider asperity height distribution than the G_W specimen in both half-spaces, indicating a larger relative asperity height. The difference is more prominent for the top half-space, i.e., the second cast block, where the asperities of the G_O specimen range in size between -0.8 and over 0.6 mm, while for the G_W top half space range between -0.6 and 0.4 mm.

3.3.4 Discussion

The aperture height and asperity height distributions can be used to explain the mechanical and geophysical response of G_O specimens during shearing (Fig. 4). At low normal stress, the apertures in the G_O specimens are connected and are larger than the apertures at 5 MPa. The G_O specimens thus required larger shear displacements than G_W specimens for the asperities to come in contact and get damaged. At higher normal stress, the apertures in the G_O specimen were still large, but less connected because of the increase in contact area. The result is that a smaller shear displacement was required to sustain damage at the microscopic level, resulting in seismic precursors to shear failure in transmitted signals, similar to what was observed in the G_W specimens. Similarly, the micro-scale data support the macro-scale observations of changes in shear strength with confinement, given that the peak shear strength of a joint is a function of normal stress, asperity strength, roughness and geometry, degree of asperity match, etc. (Barton and Choubbey 1977; Zhao 1997; Wang et al. 2020). At the lower normal stress of 2 MPa, the discontinuity in the G_O specimen had a large mismatch due to the large voids, which would call for a smaller strength compared to the G_W specimen that had a well matched discontinuity. However, the strength of the asperities in the G_O specimen was larger than in the G_W specimen as observed from the micro-indentation measurements (Fig. 8). These two factors in the G_O specimen oppose each other resulting in a peak shear strength similar to that observed in the G_W specimen. At

the larger confinement of 5 MPa, however, the discontinuity in the G_O specimen had better contact, with the number and size of the voids smaller than at 2 MPa, the asperities still had a larger strength than in the G_W specimen, thus resulting in a peak shear strength of the G_O discontinuity larger than that of the G_W specimen. Given that the micro-scale measurements show that asperity contacts in the G_O specimen do not increase linearly with normal stress, it is expected that the shear strength of the discontinuity would not have a linear dependence on normal stress (contrary to what is presented in Fig. 3, which shows a linear dependence of shear stress on normal stress).

4 Conclusions

The ability to detect seismic precursors to shear failure along rock discontinuities is extremely important but has so far only been observed on well-matched rock surfaces. It is essential to study different rock discontinuity conditions that may be present in the field, where both matched and mismatched discontinuities exist. Based on the experimental results presented in this paper, seismic precursors to shear failure, in the form of peaks in the normalized transmitted amplitudes, were detected for well-matched rock discontinuities at normal stresses of 2 and 5 MPa. Conversely, the ability to detect seismic precursors to shear failure on specimens with mismatched discontinuities (G_O specimens) was only possible at higher normal stress (5 MPa). Characterization of the joint surfaces prepared with a water-based release agent (G_W specimen) and an oil-based release agent (G_O specimen) support the hypothesis that differences the properties of the joint surface affect the onset of asperity damage. Differences in asperity micro-strength, height, and aperture distribution—degree of mismatch—influence the peak shear strength of a discontinuity and the ability to detect seismic precursors to shear failure.

Results of asperity characterization at the micro-scale show that: (1) at lower normal stress, 2 MPa for a G_O specimen, the void aperture of the (mismatched) discontinuity is large, so significant shear displacement is needed to interlock and damage the asperities; and (2) the micro-hardness of asperities was larger than that of the asperities of the (well-matched) G_W specimen, thus involving smaller damage at the same shear displacement. Both mechanisms point towards the need for large shear displacements of mismatched discontinuities asperities to induce damage, which is consistent with the inability in the experiments to detect seismic precursors to shear failure at low normal stresses. The laboratory results also indicate that there should be a threshold in the normal stress when the contact of the mismatched discontinuity is sufficient for the damage to the asperities to occur early enough, such that precursors to the macroscopic shear failure can be detected. A mismatched discontinuity is a proxy of a weathered discontinuity in the

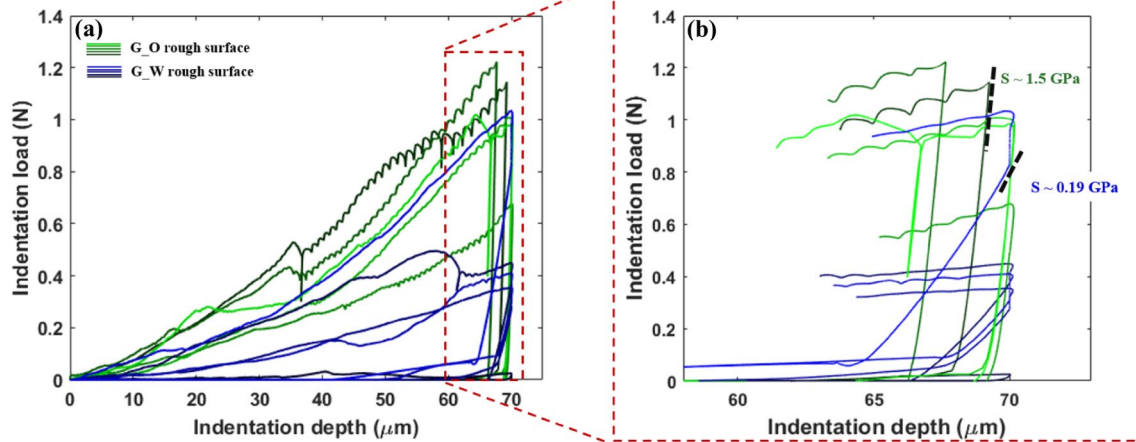


Fig. 12 Micro-indentation: **a** load–displacement curves for rough surfaces of G_W and G_O specimens; and **b** enlarged view of the unloading portion of the curves

field. Future work should include shear experiments on different types of naturally weathered rock discontinuities to understand the behavior of various types of mismatched discontinuities subjected to shear. We acknowledge that the scope of our study considers textural and physical mismatches in discontinuities and does not encompass the full range of discontinuity mismatches. Nevertheless, the study provides a fundamental understanding of the behavior of mismatched discontinuities under shear stress. We see our work as a foundational step towards future studies that could explore additional aspects of mismatched discontinuities, such as infilled discontinuities, for example.

Appendix

Micro-indentation Curves

Figure 12 shows the indentation curves obtained from micro-indenting G_W (shades of blue) and G_O (shades of green) rough surfaces (grit 36 sandpaper roughness). Almost all curves exhibit “jumps”, which are associated with the indenter coming in contact with powder produced while indenting the gypsum surface. In most tests, the load required to reach an indentation depth of $\approx 70 \mu\text{m}$ was larger for the G_O (0.7–1.1 N) specimen, indicating a surface harder than the G_W sample ($< 0.4 \text{ N}$; only one test recorded a load of $\approx 1 \text{ N}$).

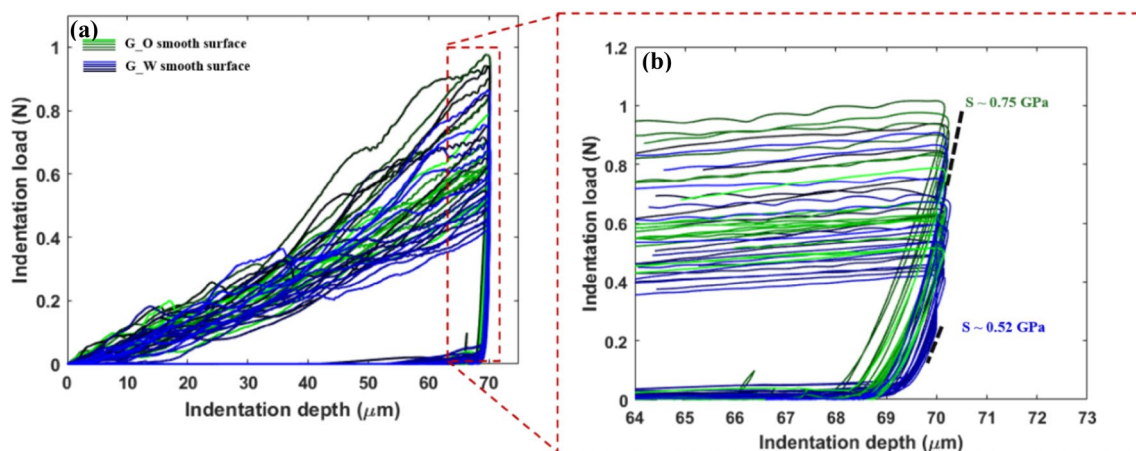


Fig. 13 Micro-indentation: **a** load–displacement curves for smooth surfaces of G_W and G_O specimens; and **b** enlarged view of the unloading portion of the curves

The load–displacement curves from the indentation tests conducted on smooth surfaces are shown in Fig. 13, where curves with shades of blue correspond to indentations performed on a G_W specimen with a smooth surface and shades of green to indentations performed on a G_O specimen, also with a smooth surface. Figure 12(b) shows an enlargement of the unloading stage of the test, for clarity. The unloading slopes were ≈ 0.75 GPa and ≈ 0.52 GPa for G_O and G_W specimens, respectively.

Acknowledgements The work presented in this paper was supported by the National Science Foundation, award number: CMMI1664562. The authors would also like to acknowledge the 3D X-Ray Microscope Facility in the Department of Physics for the images of specimens shown in this paper, which were acquired on a Zeiss Xradia 510 Versa 3D X-ray Microscope that was supported by the EVPRP Major Multi-User Equipment Program 2017 at Purdue University. The authors would like to thank Ms. Alexandra Loaiza for her help conducting the micro-indentation tests. The authors would also like to thank Dr. Christopher J. Gilpin, director of the life science microscopy facility at Purdue University for his help with the Monte Carlo simulations, to determine the electron trajectory in the EDX scans.

Author Contributions Conceptualization: HEF, AB and LJP-N; methodology: HEF, AB and LJP-N; formal analysis and investigation: HEF, AB and LJP-N; writing—original draft preparation: HEF, AB and LJP-N; writing—review and editing: HEF, AB and LJP-N; supervision: AB and LJP-N.

Data availability The data used in this study are available from the corresponding author upon reasonable request.

Declarations

Conflict of Interest The authors have no competing interests to declare that are relevant to the content of this article.

References

- ASTM International (2005) ASTM E384-05: standard test method for microindentation hardness of materials. ASTM Standard
- ASTM International (2007) ASTM E2546-07: standard practice for instrumented indentation testing. ASTM Standard
- Barton N, Choubey V (1977) The shear strength of rock joints in theory and practice. *Rock Mech* 10(1–2):1–54. <https://doi.org/10.1007/BF01261801>
- Bobet A (1998) Fracture coalescence in rock materials: experimental observations and numerical predictions. <https://elibrary.ru/item.asp?id=5532406>
- Bobet A, Einstein HH (1998) Fracture coalescence in rock-type materials under uniaxial and biaxial compression. *Int J Rock Mech Min Sci*. [https://doi.org/10.1016/S0148-9062\(98\)00005-9](https://doi.org/10.1016/S0148-9062(98)00005-9)
- Chen WY, Lovell CW, Haley GM, Pyrak-Nolte LJ (1993) Variation of shear-wave amplitude during frictional sliding. *Int J Rock Mech Min Sci*. [https://doi.org/10.1016/0148-9062\(93\)90022-6](https://doi.org/10.1016/0148-9062(93)90022-6)
- Cheng Tang Z, Ngai L, Wong Y (2016) New criterion for evaluating the peak shear strength of rock joints under different contact states. *Rock Mech Rock Eng* 49:1191–1199. <https://doi.org/10.1007/s00603-015-0811-1>
- Choi M (2013) Characterization of fractures subjected to normal and shear stress
- Choi MK, Bobet A, Pyrak-Nolte LJ (2014) The effect of surface roughness and mixed-mode loading on the stiffness ratio κ_x/κ_z for fractures. *Geophysics*. <https://doi.org/10.1190/GEO2013-0438.1>
- Combes J, Grossmann A, Tchamitchian P (1989) Wavelets: Time-Frequency Methods and Phase Space Proceedings of the International Conference, Marseille, France, December 14–18, 1987
- Demers H, Horny P, Gauvin R, Lifshin E (2002) WinX-ray: a new monte carlo program for the simulation of x-ray and charging materials. *Microsc Microanal* 8(S02):1498–1499. <https://doi.org/10.1017/S1431927602104120>
- El Fil H, Pyrak-Nolte LJ, Bobet A (2021) Transmitted, reflected, and converted modes of seismic precursors to shear failure of rock discontinuities. *Onepetro.Org*
- Fischer-Cripps AC (2011) Scaling relationships in nanoindentation. Springer, New York, pp 119–123. https://doi.org/10.1007/978-1-4419-9872-9_6
- Geurts P, Ernst D (2006) Extremely randomized trees, vol 63. Springer, pp 3–42
- Gheibi A, Li H, Hedayat A (2021) Detection of seismic precursors in converted ultrasonic waves to shear failure of natural sandstone rock joints. *Rock Mech Rock Eng* 54(7):3611–3627. <https://doi.org/10.1007/S00603-021-02507-X>
- Hedayat A (2013) Mechanical and geophysical characterization of damage in rocks. <https://docs.lib.purdue.edu/dissertations/AAI3604877/>
- Hedayat A, Hinton J (2017) Geophysical waveform's frequency attenuation as a precursor to rock shear failure. *Geotechn Spec Pub*. <https://doi.org/10.1061/9780784480472.067>
- Hedayat A, Walton G (2017) Laboratory determination of rock fracture shear stiffness using seismic wave propagation and digital image correlation. *Geotech Test J* 40(1):92–106. <https://doi.org/10.1520/GTJ20160035>
- Hedayat A, Pyrak-Nolte LJ, Bobet A (2014) Precursors to the shear failure of rock discontinuities. *Geophys Res Lett*. <https://doi.org/10.1002/2014GL060848>
- Hoek E, Brown ET (1980) Empirical strength criterion for rock masses. *J Geotech Eng Div* 106(9):1013–1035
- Hulbert C, Rouet-Leduc B, Johnson PA, Ren CX, Rivière J, Bolton DC, Marone C (2019) Similarity of fast and slow earthquakes illuminated by machine learning. *Nat Geosci*. <https://doi.org/10.1038/s41561-018-0272-8>
- Johnson PA, Rouet-Leduc B, Pyrak-Nolte LJ, Beroza GC, Marone CJ, Hulbert C, Howard A, Singer P, Gordeev D, Karaflos D, Levinson CJ, Pfeiffer P, Puk KM, Reade W (2021) Laboratory earthquake forecasting: a machine learning competition. *Proc Natl Acad Sci* 118(5):e2011362118. <https://doi.org/10.1073/PNAS.2011362118>
- Kulatilake PH, Shou G, Huang TH, Morgan RM (1995) New peak shear strength criteria for anisotropic rock joints. Elsevier
- Modiriasari A, Pyrak-Nolte LJ, Bobet A (2018) Emergent wave conversion as a precursor to shear crack initiation. *Geophys Res Lett*. <https://doi.org/10.1029/2018GL078622>
- Modiriasari A, Bobet A, Pyrak-Nolte LJ (2020) Seismic wave conversion caused by shear crack initiation and growth. *Rock Mech Rock Eng*. <https://doi.org/10.1007/s00603-020-02079-2>
- Mutlu O, Bobet A (2006) Slip propagation along frictional discontinuities. *Int J Rock Mech Min Sci*. <https://doi.org/10.1016/j.ijrmmms.2005.11.012>
- Nakagawa S, Nihei KT, Myer LR (2000) Shear-induced conversion of seismic waves across single fractures. *Int J Rock Mech Min Sci*. [https://doi.org/10.1016/S1365-1609\(99\)00101-X](https://doi.org/10.1016/S1365-1609(99)00101-X)
- Nolte DD, Pyrak-Nolte LJ (2022) Monitoring fracture saturation with internal seismic sources and twin neural networks. *J Geophys Res Solid Earth*. <https://doi.org/10.1029/2021JB023005>
- Nolte DD, Pyrak-Nolte LJ, Beachy J, Ziegler C (2000) Transition from the displacement discontinuity limit to the resonant scattering

- regime for fracture interface waves. *Int J Rock Mech Min Sci*. [https://doi.org/10.1016/S1365-1609\(99\)00102-1](https://doi.org/10.1016/S1365-1609(99)00102-1)
- Pyrak-Nolte LJ (2018) Fracture specific stiffness. *Science of carbon storage in deep saline formations: process coupling across time and spatial scales*. Elsevier
- Pyrak-Nolte LJ, Myer LR, Cook NGW (1990) Transmission of seismic waves across single natural fractures. *J Geophys Res*. <https://doi.org/10.1029/JB095iB06p08617>
- Rouet-Leduc B, Hulbert C, Lubbers N, Barros K, Humphreys CJ, Johnson PA (2017) Machine learning predicts laboratory earthquakes. *Geophys Res Lett*. <https://doi.org/10.1002/2017GL074677>
- Scuderi MM, Marone C, Tinti E, di Stefano G, Collettini C (2016) Precursory changes in seismic velocity for the spectrum of earthquake failure modes. *Nat Geosci*. <https://doi.org/10.1038/ngeo2775>
- Singh HK, Basu A (2016) Shear behaviors of 'real' natural un-matching joints of granite with equivalent joint roughness coefficients. *Eng Geol*. <https://doi.org/10.1016/j.enggeo.2016.07.004>
- Singh HK, Basu A (2018) A comparison between the shear behavior of 'real' natural rock discontinuities and their replicas. *Rock Mech Rock Eng* 51(1):329–340. <https://doi.org/10.1007/S00603-017-1334-8>
- Tiwari A, Sain K, Kumar A, Tiwari J, Paul A, Kumar N, Haldar C, Kumar S, Pandey CP (2022) Potential seismic precursors and surficial dynamics of a deadly Himalayan disaster: an early warning approach. *Sci Rep* 12:3733. <https://doi.org/10.1038/s41598-022-07491-y>
- Wang C, Elsworth D, Fang Y, Zhang F (2020) Influence of fracture roughness on shear strength, slip stability and permeability: a mechanistic analysis by three-dimensional digital rock modeling. Elsevier
- Xia CC, Tang ZC, Xiao WM, Song YL (2014) New peak shear strength criterion of rock joints based on quantified surface description. *Rock Mech Rock Eng* 47(2):387–400. <https://doi.org/10.1007/S00603-013-0395-6>
- Zhao J (1997) Joint surface matching and shear strength. Part A: joint matching coefficient (JMC). *Int J Rock Mech Min Sci Geomech Abstracts* 34(2):173–178. [https://doi.org/10.1016/S0148-9062\(96\)00062-9](https://doi.org/10.1016/S0148-9062(96)00062-9)

Publisher's Note Springer Nature remains neutral with regard to jurisdictional claims in published maps and institutional affiliations.

Springer Nature or its licensor (e.g. a society or other partner) holds exclusive rights to this article under a publishing agreement with the author(s) or other rightsholder(s); author self-archiving of the accepted manuscript version of this article is solely governed by the terms of such publishing agreement and applicable law.